Boundary-Layer Instabilities Over a Cone-Cylinder-Flare Model at Mach 6

Pedro Paredes, *
National Institute of Aerospace, Hampton, VA 23666, USA

Anton Scholten, †
North Carolina State University, Raleigh, NC 27695, USA

Meelan M. Choudhari, ‡ Fei Li, §
NASA Langley Research Center, Hampton, VA 23681, USA

Elizabeth K. Benitez, ¶
U.S. Air Force Research Laboratory, Wright-Patterson Air Force Base, OH, 45433

Joseph S. Jewell ‖
Purdue University, West Lafayette, IN, 47907

Computations are performed to investigate the boundary-layer instabilities over a sharp cone-cylinder-flare model at zero degrees angle of attack. The model geometry and the flow conditions are selected to match the experiments conducted in the Boeing/AFOSR Mach 6 Quiet Tunnel (BAM6QT) at Purdue University. The geometry consists of a nominally sharp 5° half-angle cone, followed by a cylindrical segment and then a 10° flare. An axisymmetric separation bubble is generated as a result of the laminar shock/boundary-layer interaction in the cylinder-flare region. The comparison of the laminar flow solution and the schlieren images shows a remarkable agreement between the respective locations of both the boundary-layer edge and the reattachment shock. The predicted heat flux distribution is also in agreement with the measured values downstream of the reattachment location. The analysis of convective and global instabilities is performed for flare half angles equal to 8°, 10°, and 12° and nosetip radii equal to 0.1, 1, and 5 mm. The linear amplification of first and second Mack mode instabilities that begin to amplify in the cone region are computed with a combination of the parabolized stability equations (PSE) and the harmonic linearized Navier-Stokes equations (HLNSE). The predicted frequency spectra of the surface pressure fluctuations associated with both planar and oblique instability waves are compared with the measured spectra at the various locations of the PCB and Kulite sensors. The comparison shows that the computational analysis captures the distinct lobes within the disturbance amplification spectra measured in the experiments, but some differences in amplification characteristics are noted at low frequencies. Overall, the oblique disturbances are found to be more amplified than the planar disturbances. To our knowledge, this represents the first successful comparison between convective instability analysis and measured surface pressure fluctuations for a hypersonic configuration with a separation bubble. Finally, the global instability analysis shows that the laminar flow becomes supercritical for flare half angles larger than 8°. The unstable global mode for the experimental configuration of a 10° flare and a sharp nosetip cone corresponds to a stationary three-dimensional disturbance that is concentrated in the recirculation region and achieves its maximum growth rate for an azimuthal wavenumber of 5.

*Senior Research Engineer, Computational AeroSciences Branch, NASA LaRC. AIAA Senior Member
†Graduate Student, Department of Mechanical and Aerospace Engineering. AIAA Student Member
‡Aerospace Technologist, Computational AeroSciences Branch. AIAA Fellow
§Aerospace Technologist, Computational AeroSciences Branch.
¶NRC Research Associate. AIAA Member
‖Assistant Professor, School of Aeronautics and Astronautics. AIAA Associate Fellow

Nomenclature

f	=	disturbance frequency [s^{-1}]
h_ξ	=	streamwise metric factor
h_ζ	=	azimuthal metric factor [m]
m	=	azimuthal wavenumber [rad^{-1}]
M	=	Mach number
N	=	logarithmic amplification factor
$\hat{\mathbf{q}}$	=	vector of amplitude variables
$\breve{\mathbf{q}}$	=	vector of disturbance function variables
$\bar{\mathbf{q}}$	=	vector of base flow variables
$\tilde{\mathbf{q}}$	=	vector of perturbation variables
Re_∞	=	freestream unit Reynolds number [m^{-1}]
r_b	=	local radius of axisymmetric body at the axial station of interest [m]
r_N	=	nose radius [m]
T	=	temperature [K]
T_w	=	wall temperature [K]
(u, v, w)	=	streamwise, wall-normal, and azimuthal velocity components [$m \cdot s^{-1}$]
(x, y, z)	=	Cartesian coordinates
α	=	streamwise wavenumber [m^{-1}]
κ	=	streamwise curvature [m^{-1}]
ω	=	disturbance angular frequency [s^{-1}]
ρ	=	density [kg m^{-3}]
(ξ, η, ζ)	=	streamwise, wall-normal, and azimuthal coordinates
Superscripts		
$*$	=	dimensional value
H	=	conjugate transpose
Subscript		
∞	=	freestream value

I. Introduction

Laminar-turbulent transition of boundary-layer flows can have a strong impact on the performance of hypersonic vehicles because of its influence on the surface skin friction and aerodynamic heating. Furthermore, deflected control surfaces or other geometric ramps lead to flow separation and reattachment due to shock-wave/boundary-layer interactions (SBLIs) that can have a significant influence on the heat flux distribution. Therefore, the prediction and control of transition onset in high-speed flows with SBLI effects are key issues for optimizing the performance of high-speed vehicles.

The viscous-inviscid interactive flow in the vicinity of a compression ramp includes an oblique shock upstream of the compression corner, along with an adverse pressure gradient that decelerates the flow and causes a thickening of the boundary layer. A recirculation region can form when the ramp angle is increased and the adverse pressure gradient becomes stronger. The experimental measurements have shown that, for sufficiently large compression angles, the incoming laminar flow can transition to turbulence ahead of the reattachment location.

The first studies on the effects of transition in the presence of shock-induced boundary-layer separation were performed during experiments at NASA Langley by Becker and Korycinsky [1]. The results indicated extensive zones of separated flow ahead of the flare when the boundary layer was laminar at separation, while the extent of the separated zone was greatly reduced in the turbulent cases. Chapman et al. [2] also studied the effect of transition on the separation due to SBLI. Their measurements indicated that the principal variable controlling the pressure distribution in the separated flow was the location of transition relative to the reattachment and separation points. A cone-cylinder-flare geometry was experimentally studied by Schaefer and Ferguson [3]. They documented the surface pressures and heat transfer in laminar, transitional, and turbulent flow at Mach 4.98. The characterization of the separation length and heat transfer for an axisymmetric cone-flare configuration at laminar, transitional, and turbulent conditions as a function of the nose bluntness, freestream Reynolds number, and flare angle has been recently reported by Running et al. [4].

A common observation in the context of transitional flow over axisymmetric and planar geometries with compression

corners is the formation of streamwise vortices or streaks in the reattached boundary layer downstream of the separation bubble. Ginoux [5] used a flat plate with a flap and a hollow cylinder with a flare in ground tests at Mach 3. The streamwise vortices were observed in the reattachment area for both models. Thereafter, the signature of streamwise vortices at the reattachment over compression ramps or flares has been documented for a variety of geometries and conditions, e.g., Refs. [6–9]. Numerical studies have investigated the global instability of laminar SBLI problems. Robinet [10] and Hildebrand et al. [11] studied the laminar shock-induced separation of flow over a flat plate at Mach 2.15 and Mach 5.92, respectively. As the angle of the oblique shock is increased, the separation length increases, and the flow becomes unstable due to a three-dimensional stationary disturbance that leads to a spanwise modulation of the flow downstream of the reattachment location. The global stability analysis of a double wedge at Mach 5 performed by GS et al. [12] also identified a stationary three-dimensional instability that became unstable beyond a certain turning angle, and the spanwise wavelength of the most unstable global mode agreed with the experimental measurements of Yang et al. [7] at a larger turning angle. However, the high-fidelity simulations of the transitional SBLIs caused by a 15° axisymmetric compression ramp at Mach 5 by Lugrin et al. [13] indicate that the reattachment streaks can also be produced by the nonlinear interaction of oblique first mode waves that continue to amplify through the shear layer over the separation region.

The evolution of boundary-layer instabilities over an axisymmetric configuration with SBLI has been recently investigated by using a cone-cylinder-flare model at zero degrees angle of attack by Esquieu et al. [14] and Benitez et al. [15] and at nonzero angles of attack by Benitez et al. [16], and with a cone-flare at zero degrees angle of attack by Butler and Laurence [17]. The cone-cylinder-flare geometry was used in the Boeing/AFOSR Mach 6 quiet tunnel (BAM6QT) at Purdue University with flare angles equal to 3.5° and 10°. The numerical and experimental results for the 3.5° flare case were presented by Esquieu et al. [14]. At the smaller flare angle of 3.5 degrees, the boundary layer remains attached, and the amplification of linear instability waves predicted by linear stability theory (LST) and parabolized stability equations (PSE) indicates favorable agreement with the measured wall-pressure power spectra. However, their LST and PSE predictions for the 10° flare configuration at zero degrees angle of attack did not capture the distinct lobes found in the measured power spectra downstream of the reattachment location [15]. Additional experimental measurements for the 10° flare configuration are presented by Benitez et al. [16] for both zero and nonzero angles of attack. The experiments of Butler and Laurence [17] with a cone-flare at zero degrees angle of attack were conducted in the University of Maryland's HyperTERP hypersonic shock tunnel. The test article consisted of a 5° half-angle cone and two interchangeable flares of 0° and 15°. The 0° expansion flare was found to stabilize the boundary-layer disturbances, while the 15° compression flare had a destabilizing effect that promoted a laminar breakdown upon reattachment.

The present paper investigates the instability characteristics of the boundary layer over a sharp cone-cylinder-flare model at zero degrees angle of attack with a 10° half-angle flare that was tested in the BAM6QT at Purdue University [15, 16]. Additionally, the nosetip radius and flare angle are varied to study their effects on the instabilitiy characteristics. The methodologies used to investigate the disturbances are summarized in Section II. The nonparallel flow effects are included to study the evolution of convective boundary-layer instabilities by the application of the harmonic linearized Navier-Stokes equations (HLNSE) that do not invoke the weakly nonparallel assumption of the PSE. A global instability analysis of the separated region is also performed to study the potential for self-excited, i.e., global, disturbances. The laminar boundary-layer flow over the selected configurations and the instability analysis of these flows are presented in Section III. A brief summary and concluding remarks are presented in Section IV.

II. Theory

In this section, we outline the methodology used for the analysis of disturbance amplification over the cone-cylinder-flare configuration. The evolution of convective instabilities is calculated with the linear parabolized stability equations (PSE) and the harmonic linearized Navier-Stokes equations (HLNSE) frameworks. The global stability analysis (GSA) of the laminar flow solution is also performed for selected flare angles and nosetip radii.

A. Governing Equations

The present work is focused on the axisymmetric boundary layers over the cone-cylinder-flare configuration of interest. The freestream conditions and geometric parameters model the experimental configuration by Benitez et al. [16] that included a sharp, 5°cone, a cylinder, and a 10° flare.

The computational coordinates are defined as an orthogonal body-fitted coordinate system along the cone region, with (ξ, η, ζ) denoting the streamwise, wall-normal, and azimuthal coordinates, respectively, and (u, v, w) representing the corresponding velocity components in the cone region. The same orientation of the coordinate system and velocities

is maintained along the cylinder and flare regions with a nonorthogonal transformation of the two-dimensional grid. The density and temperature are denoted by ρ and T, respectively. The curvature metric factors associated with the streamwise and azimuthal curvature, respectively, are defined as

$$h_\xi = 1 + \kappa\eta, \tag{1}$$

$$h_\zeta = r_b + \eta\cos(\theta), \tag{2}$$

where κ denotes the streamwise curvature, r_b is the local radius, and θ is the local half angle along the axisymmetric surface, i.e., $\sin(\theta) = dr_b/d\xi$. The Cartesian coordinates are represented by (x, y, z). The vector of basic state variables corresponds to $\bar{\mathbf{q}}(\xi,\eta,\zeta) = (\bar{\rho},\bar{u},\bar{v},\bar{w},\bar{T})^T$ and the vector of perturbation variables is denoted by $\tilde{\mathbf{q}}(\xi,\eta,\zeta,t) = (\tilde{\rho},\tilde{u},\tilde{v},\tilde{w},\tilde{T})^T$. For axisymmetric geometries at zero degrees angle of attack, the basic state variables are independent of the azimuthal coordinate and the linear perturbations can be assumed to be harmonic in time and in the azimuthal direction, which leads to the following expression for the perturbations,

$$\tilde{\mathbf{q}}(\xi,\eta,\zeta,t) = \breve{\mathbf{q}}(\xi,\eta)\exp\left[\mathrm{i}\left(m\zeta - \omega t\right)\right] + \text{c.c.}, \tag{3}$$

where the vector of disturbance functions is $\breve{\mathbf{q}}(\xi,\eta,\zeta) = (\breve{\rho},\breve{u},\breve{v},\breve{w},\breve{T})^T$, m is the azimuthal wavenumber, ω is the angular frequency, and c.c. refers to the complex conjugate.

The disturbance functions $\breve{\mathbf{q}}(\xi,\eta,\zeta)$ satisfy the HLNSE [18], which involve coefficient functions that depend on the basic state variables and parameters, and on the angular frequency and azimuthal wavenumber of the perturbation,

$$\mathbf{L}_{HLNSE}\,\breve{\mathbf{q}}(\xi,\eta) = \breve{\mathbf{f}}, \tag{4}$$

where $\breve{\mathbf{f}}$ represents a potential forcing term.

The PSE approximation to the HLNSE is based on isolating the rapid phase variations in the streamwise direction by introducing the disturbance ansatz

$$\breve{\mathbf{q}}(\xi,\eta,\zeta) = \hat{\mathbf{q}}(\xi,\eta,\zeta)\exp\left[\mathrm{i}\int_{\xi_0}^{\xi}\alpha(\xi')\,\mathrm{d}\xi'\right], \tag{5}$$

where the unknown, streamwise varying wavenumber $\alpha(\xi)$ is determined in the course of the solution by imposing an additional constraint

$$\int_\eta \hat{\mathbf{q}}^*\frac{\partial\hat{\mathbf{q}}}{\partial\xi}\,h_\xi\,h_\zeta\,\mathrm{d}\eta\,\mathrm{d}\zeta = 0, \tag{6}$$

and requiring the amplitude functions $\hat{\mathbf{q}}(\xi,\eta,\zeta) = (\hat{\rho},\hat{u},\hat{v},\hat{w},\hat{T})^T$ to vary slowly in the streamwise direction in comparison with the phase term $\exp\left[\mathrm{i}\int_{\xi_0}^{\xi}\alpha(\xi')\,\mathrm{d}\xi'\right]$. Substituting Eq. (5) into the HLNSE and invoking scale separation between the streamwise coordinate and the other two directions to neglect the viscous terms with streamwise derivatives, the PSE are obtained in the form

$$\left(\mathbf{L}_{PSE} + \mathbf{M}_{PSE}\frac{1}{h_\xi}\frac{\partial}{\partial\xi}\right)\hat{\mathbf{q}}(\xi,\eta) = 0. \tag{7}$$

The onset of laminar-turbulent transition is estimated by using the logarithmic amplification ratio, the so-called N-factor, relative to the location ξ_I where the disturbance first becomes unstable,

$$N_\phi = -\int_{\xi_I}^{\xi}\alpha_i(\xi')\,\mathrm{d}\xi' + \ln\left[\hat{\phi}(\xi)/\hat{\phi}(\xi_I)\right]. \tag{8}$$

Here, $\hat{\phi}$ denotes an amplitude norm of $\hat{\mathbf{q}}$ at a given ξ, e.g., wall-pressure disturbance or total disturbance energy [19, 20].

The global stability analysis (GSA) is based on the HLNSE, with the real-valued angular frequency ω from Eq. (3) replaced by a complex value $\Omega = \omega + \mathrm{i}\sigma$, where σ is the temporal growth rate of the disturbance. After setting $\breve{\mathbf{f}} = 0$ and defining $\hat{\mathbf{q}} \equiv \breve{\mathbf{q}}$, Eq. (4) can be written as the generalized eigenvalue problem,

$$\mathbf{A}\hat{\mathbf{q}} = \Omega\mathbf{B}\hat{\mathbf{q}}, \tag{9}$$

where the leading eigenvalues Ω and eigenvectors $\hat{\mathbf{q}}$ are calculated with the Arnoldi algorithm [21].

B. Discretization and Boundary Conditions

High-order finite-difference schemes [22, 23] of sixth order are used to discretize the stability equations on a nonuniform grid along the the wall-normal direction. For the results presented here, the wall-normal direction is discretized with $N_\eta = 201$, with the nodes clustered toward the wall. The discretized PSE are integrated along the streamwise coordinate by using second-order backward differentiation. The HLNSE and the GSA equations are discretized with $N_\xi = 2001$ points along the streamwise coordinate by using centered, sixth-order finite differences. The number of discretization points in both directions is varied in selected cases to ensure the numerical convergence of the results.

No-slip, isothermal boundary conditions are used at the wall, i.e., $\hat{u} = \hat{v} = \hat{w} = \hat{T} = 0$. The farfield boundary is set just below the shock layer, and the amplitude functions are forced to decay at the farfield boundary by imposing the Dirichlet conditions $\hat{\rho} = \hat{u} = \hat{w} = \hat{T} = 0$. For the HLNSE, the inflow condition is based on the solution of the PSE, and the perturbations are forced to decay at the outflow boundary with an sponge region. For the GSA, the sponge is imposed at both inflow and outflow boundaries.

III. Results

This section begins with the presentation of the laminar flow solution over a cone-cylinder-flare model at zero degrees angle of attack in a Mach 6 free stream. The forebody section has a nominally sharp nose, and a 5° half angle, whereas the flare half angle corresponds to 10°. The basic state description is followed by results pertaining to the evolution of both planar and oblique disturbances in the boundary layer, as well as to the global instability characteristics of the laminar flow as a function of the nosetip radius and the flare half angle.

A. Laminar Boundary-Layer Flow

The present configuration is selected to match the experiments conducted by Benitez et al. [15, 16] in the Boeing/AFOSR Mach 6 Quiet Tunnel (BAM6QT) at Purdue University. The BAM6QT maintains a laminar nozzle wall boundary layer, greatly reducing the freestream noise levels in comparison with conventional facilities. These reduced noise levels are believed to be comparable to those in the flight conditions. The BAM6QT is designed as a Ludwieg tube that is capable of being run with either noisy or quiet flow, with run times of up to 6 seconds. The working fluid is air, and the effects of chemistry and molecular vibration are negligible. A detailed description of the BAM6QT facility is given by Schneider [24]. The experimental measurements were taken with PCB® piezotronics pressure sensors, Kulite® pressure transducers, infrared thermography, schlieren images, and focused laser differential interferometry (FLDI). The geometric details of the model used in the experiments are shown in Fig. 1. The model is divided into three components: a stainless steel nosetip, an aluminum cone-cylinder, and a Polyether Ether Ketone (PEEK) cylinder-flare. The instrumentation includes ports for up to 33 PCB® sensors, with 14 along the central sensor ray, 4 located ±5° away on each side of the central sensor, and the remaining 15 sensors at 90° intervals from each other around the circumference of the model. Additionally, there are 14 ports for Kulite® sensors, located 30° from the central ray of sensors.

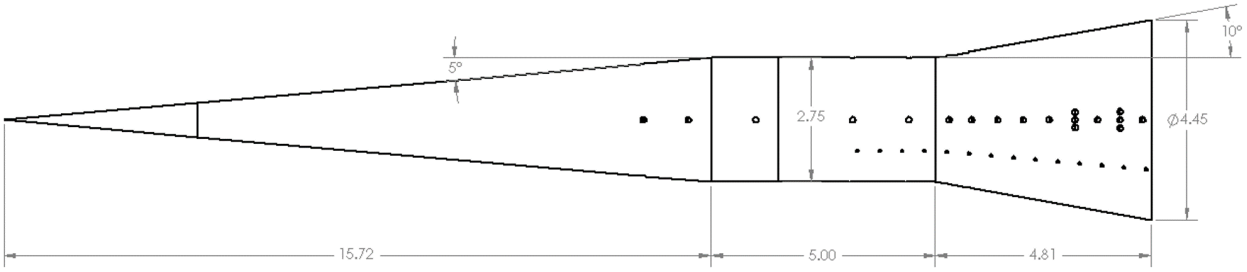

Fig. 1 Sketch of the cone-cylinder-flare model used in experiments from Refs. [15, 16]. Lengths are in inches, and angles in degrees.

The laminar basic states over the cone-cylinder-flare geometry are computed for a selected set of freestream conditions by using a second-order accurate algorithm as implemented in the finite-volume compressible Navier-Stokes

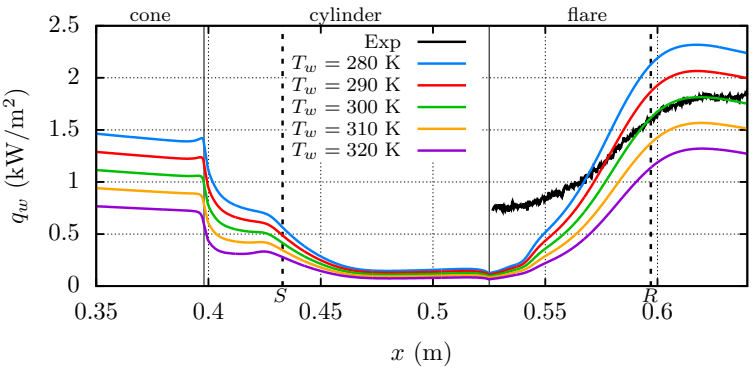

Fig. 2 Axial evolution of surface heat flux corresponding to the laminar flow solution over the sharp cone-cylinder-flare geometry with 10° flare half angle for selected wall temperatures and its comparison with the experimental measurements [16]. The vertical dashed lines denote the separation (S) and reattachment (R) locations. The vertical solid lines at $x = 0.399$ m and 0.526 m denote the cone-cylinder and cylinder-flare corners, respectively.

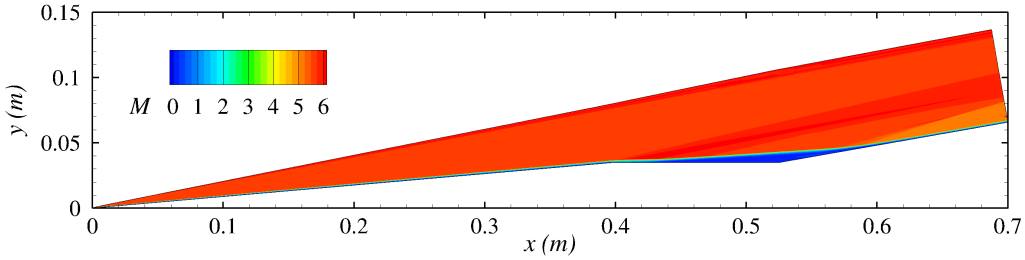

Fig. 3 Mach number contours of the laminar flow solution over the cone-cylinder-flare geometry with 10° flare half angle.

flow solver VULCAN-CFD* [25]. The VULCAN-CFD solution is based on the full Navier-Stokes equations and uses the solver's built-in capability to iteratively adapt the computational grid to the bow shock. Sutherland's law for air is used to calculate the dynamic viscosity as a function of temperature. The freestream conditions are selected to match those of the experiments, i.e., a Mach 6.0 flow with a unit Reynolds number of 11.5×10^6 m^{-1}, freestream temperature of $T^*_\infty = 51.4$ K, freestream density of $\rho^*_\infty = 0.04429$ kg/m^3, and an isothermal wall with $T^*_w = 300$ K. The sharp nosetip is modeled with a radius of $r^*_n = 0.1$ mm as measured by Benitez et al. [16]. The computational grid is composed of 3601×1201 points with enough points clustered next to the model surface to resolve the thickness of the boundary layer. The grid resolution is selected based on the convergence of the stability results by using a coarser grid with 2401×801 points and a finer grid with 4801×1601 points. The selection of the wall temperature is based on the comparison shown in Fig. 2 of the wall heat transfer results with the experimental heat transfer data that are available over the flare surface. For $T^*_w = 300$ K, there is a remarkable agreement between the predicted and measured heat flux distributions in the region downstream of the reattachment location.

The Mach number contours based on the laminar flow solution are shown in Fig. 3. The density isolines are superimposed with the schlieren images from the experiment in Fig. 4. To allow for a meaningful comparison, the schlieren images are adjusted such that the cylinder-flare corner coincides with that in the computed solution, and the length of the solid orange line corresponds to 8.2 *mm*, which is equal to the boundray-layer thickness at that location. The separation shock, the boundary-layer edge, the shear layer over the separation region, and the reattachment shock observed in the schlieren images are seen to be well-aligned with the clustering of the density isolines from the computed solution.

*visit `http://vulcan-cfd.larc.nasa.gov` for further information about the VULCAN-CFD solver

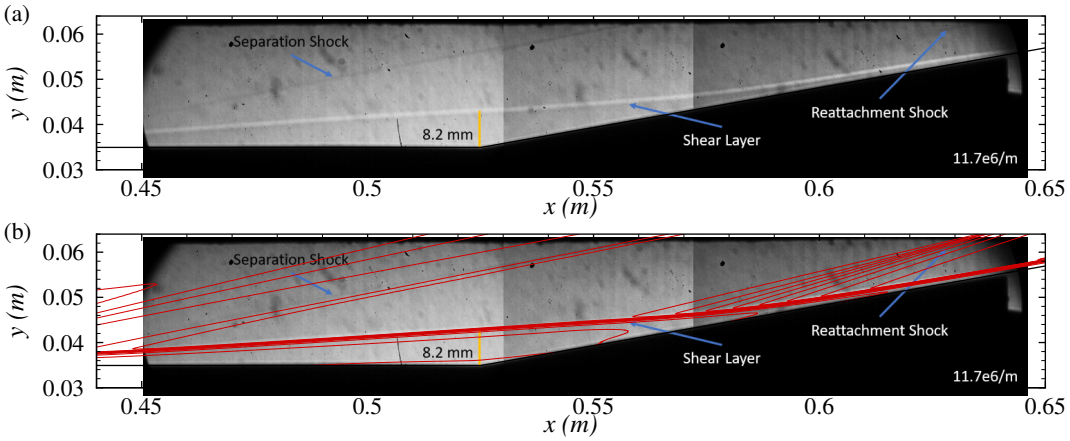

Fig. 4 Schlieren images (a) without and (b) with superposition of density isolines of the laminar flow solution over the sharp cone-cylinder-flare geometry with 10° flare half angle.

B. Convective Instabilities

The evolution of convective boundary-layer instabilities is analyzed with a hybrid methodology comprised of PSE and HLNSE solutions across overlapping streamwise domains. The linear amplification of planar and oblique, first and second Mack mode disturbances along the cone is computed with PSE until just upstream of the cone-cylinder juncture. The HLNSE are used to calculate the development of the instability waves through the remaining length of the geometry. The inflow condition for the integration of the HLNSE is based on the solution of the PSE at $x = 0.35$ m, i.e., upstream of the cone-cylinder junction that is located at $x = 0.399$ m.

Figures 5 and 6 show the comparison of the power spectra from the PCB® and Kulite® sensors, respectively, and the spectra calculated with the linear N-factor values based on the amplitudes of the wall pressure disturbance, $A_{p_w} = A_I \exp(N_{p_w})$, where the initial disturbance amplitude is selected equal to $A_I = 7.4 \times 10^{-11}$ for all selected disturbances so as to match the peak value of the predicted amplitude spectra with the measured peak amplitude at $x = 0.387$ m. Figure 5(a) shows that the most amplified instabilities at $x = 0.387$ m correspond to oblique modes with $m = 10$. The peak frequency near 220 kHz as well as the frequency bandwidth of the amplified disturbances is in agreement with the measured spectra. The next downstream PCB® sensor is located at $x = 0.511$ m, i.e., near the cylinder-flare juncture and within the recirculation region (Fig. 5(b)). The measured wall-pressure signal at this location is dominated by electrical noise, and no disturbance peaks are visible in the spectra. The calculations also predict a reduction in the amplitudes of the high frequency disturbances in the vicinity of $f = 210$ kHz, bringing the peak disturbance amplitude across this lobe well below the sensor electronic noise level. The computations also predict the emergence of a new overall peak in the range of $f = (30, 120)$ kHz; however, those amplitudes are also predicted to be below the measured background noise levels, in agreement with the absence of this peak from the measured spectrum. Downstream of the reattachment location at $x = 0.606$ m (Fig. 5(c)), the disturbance levels across both the low- and high-frequency bands are predicted to be well above the noise levels and, again, the estimated peak frequencies of both lobes and the corresponding frequency bandwidths agree well with the measurements. The peak disturbance amplitudes corresponding to each lobe are also comparable to each other, and the measured spectra confirm the predicted trend that the low-frequency peak is stronger at this station. Similar observations may be made from the comparison of the wall-pressure spectra in Figs. 5(d), 5(e), and 5(f) for locations $x = 0.619$ m, 0.631 m, and 0.643 m, respectively. The calculations show the rise of a third distinct lobe around $f = 70$ kHz at $x = 0.619$ m, which is also seen in both the measured and calculated spectra at the next sensor location of $x = 0.631$ m. Again, at the last station shown in Fig. 5(f), i.e., $x = 0.643$ m, two distinct lobes are observed in both the measured and the calculated spectra. The comparison of the predicted disturbance amplification spectra with the Kulite® measurements of Fig. 6 indicates a favorable agreement with the predicted peak frequencies and the bandwidths of the corresponding lobes, as well as highlighting an overestimation of the amplification factors at low frequencies. The low frequency disturbances in the range of $f = (30, 150)$ kHz originate from oblique first modes, and their amplitudes indicate a nonmonotonic evolution downstream of the reattachment location, i.e., for $x > 0.58$ m. However, the higher frequency disturbances in the range $f = (180, 250)$ kHz that were initiated as Mack's second mode instabilities continue to amplify across the downstream region of $x > 0.58$ m.

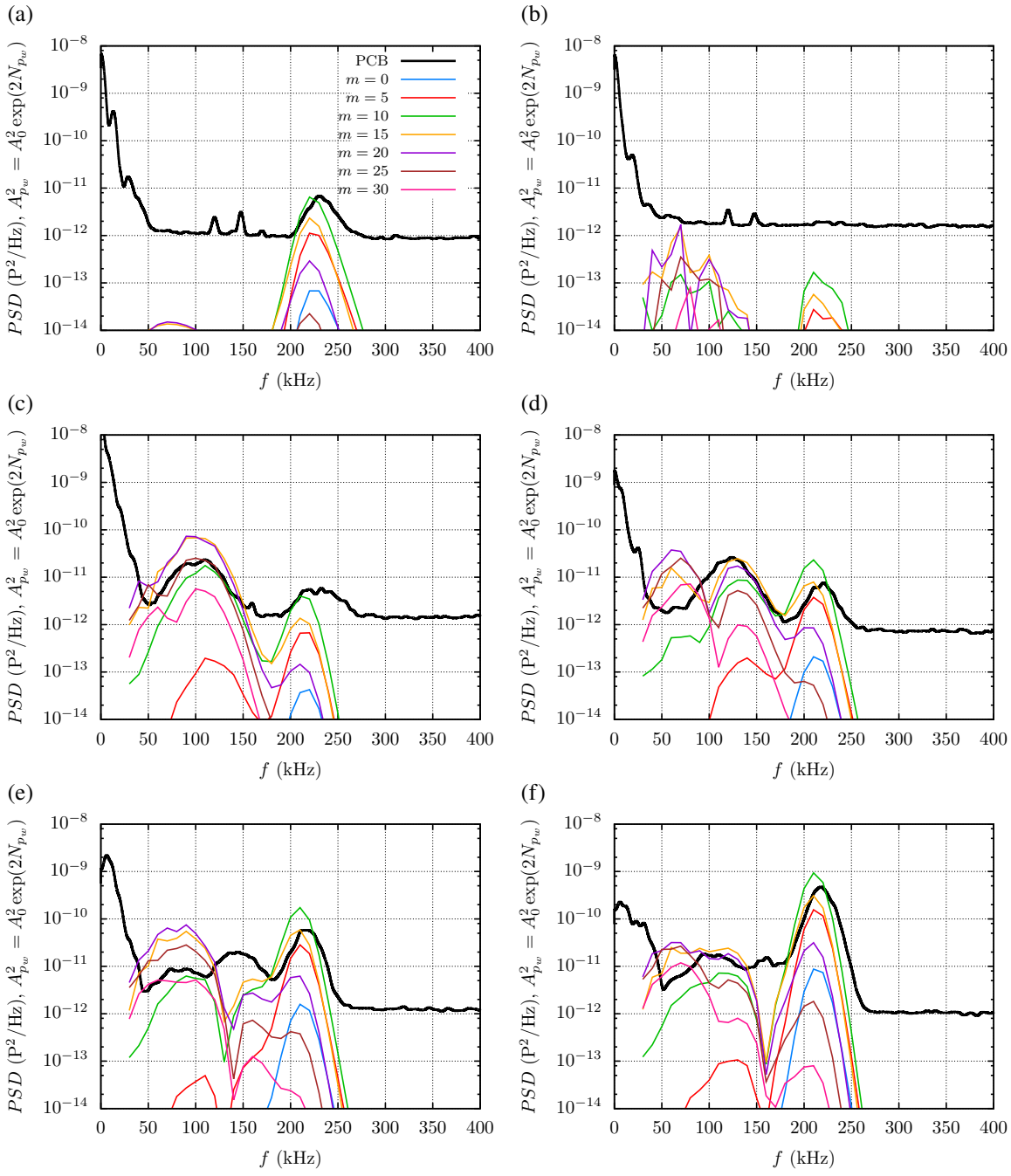

Fig. 5 Power spectra from PCB® measurements and wall-pressure disturbance spectra associated with the linear amplification of planar and oblique waves with $A_{p_w} = A_I \exp(N_{p_w})$, $A_I = 7.4 \times 10^{-11}$. The locations are (a) $x = 0.387$ m, (b) $x = 0.511$ m, (c) $x = 0.606$ m, (d) $x = 0.619$ m, (e) $x = 0.631$ m, (f) $x = 0.643$ m.

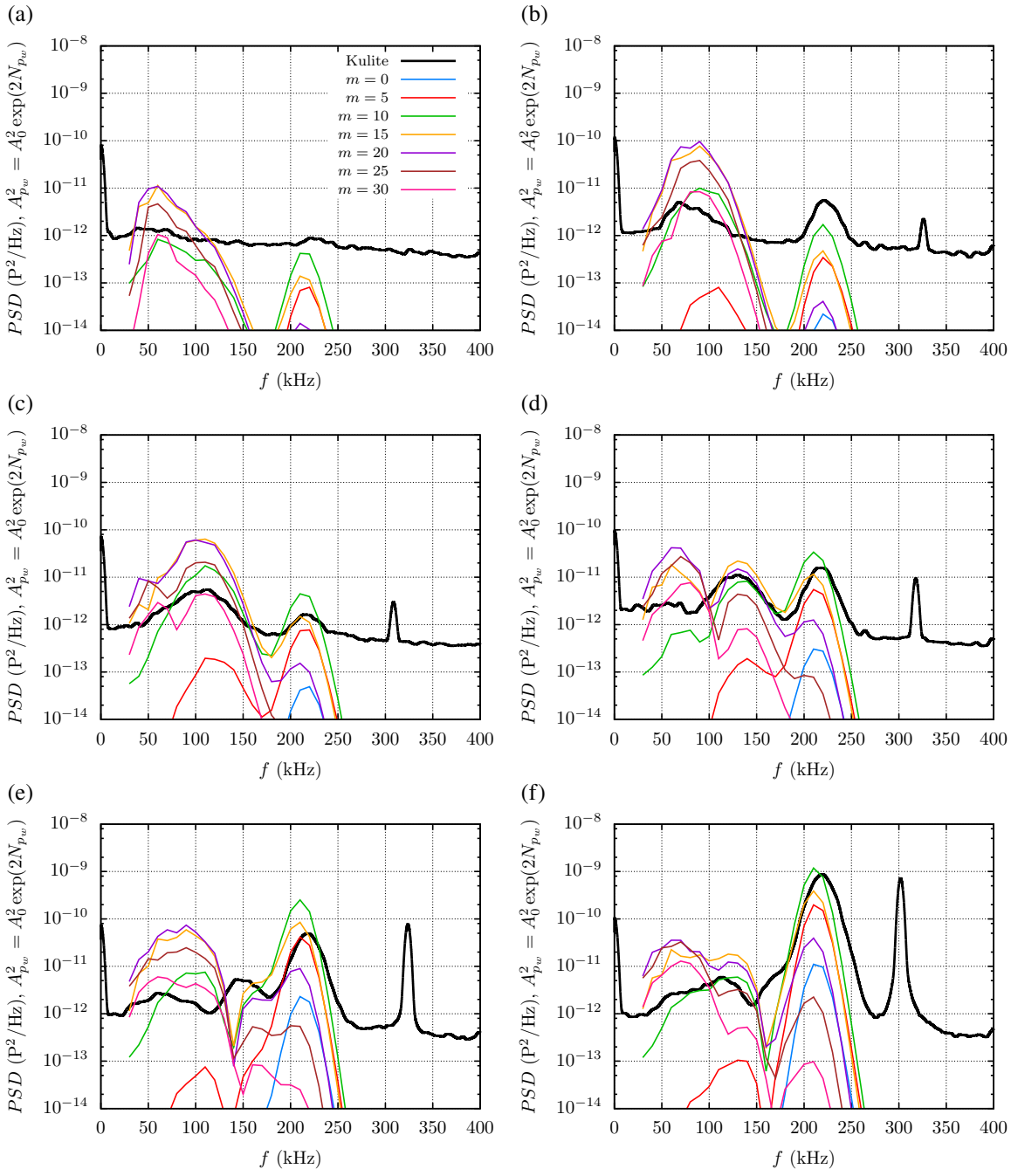

Fig. 6 Power spectra from Kulite® measurements and wall-pressure disturbance spectra associated with the linear amplification of planar and oblique waves with $A_{p_w} = A_I \exp(N_{p_w})$, $A_I = 7.4 \times 10^{-11}$. The locations are (a) $x = 0.570$ m, (b) $x = 0.595$ m, (c) $x = 0.608$ m, (d) $x = 0.620$ m, (e) $x = 0.633$ m, (f) $x = 0.645$ m.

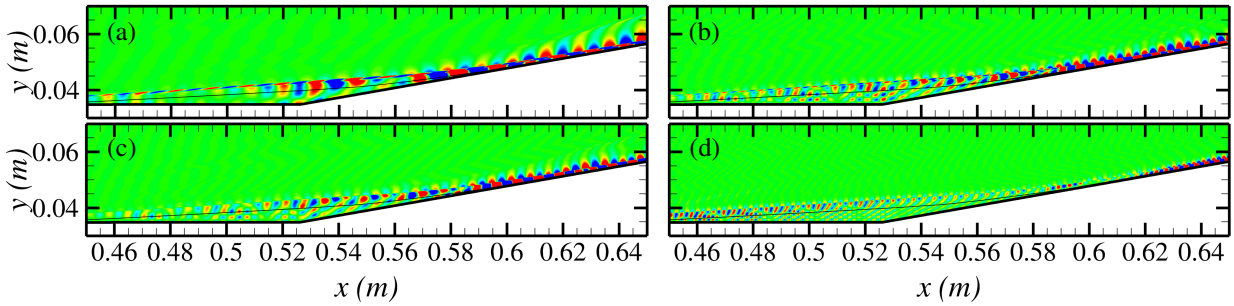

Fig. 7 Contours of real part of streamwise velocity perturbation ($\Re(\hat{u})$) for disturbances with (a) $f = 60$ kHz, $m = 20$, (b) $f = 120$ kHz, $m = 20$, (c) $f = 110$ kHz, $m = 0$, and (d) $f = 210$ kHz, $m = 0$. The colormap ranges from blue for negative values to red for positive values.

The mode shape evolution of selected disturbances across the recirculation region in the range $x = (0.45, 0.65)$ m is plotted in Fig. 7. The oblique disturbances with $m = 20$ and frequencies of $f = 60$ kHz and $f = 120$ kHz as shown in Figs. 7(a) and 7(b), respectively, continue to amplify over the recirculation bubble with peak fluctuation levels near the boundary-layer edge. The disturbance signature in the near-wall region is observed to be rather weak within the separated region. The planar waves ($m = 0$) with $f = 110$ kHz and $f = 210$ kHz from Figs. 7(c) and 7(d), respectively, do not show the peak near the boundary-layer edge over the separated region. The disturbance amplitude continues to increase downstream of the reattachment location for the $f = 210$ kHz wave, but the amplitude of the lower frequency wave with $f = 110$ kHz remains nearly flat for $x > 0.58$ m.

The effects of the flare half angle on the amplification of the boundary-layer instabilities are examined by performing the same hybrid PSE and HLNSE calculation for the cone-cylinder-cone configurations with a sharp cone and a lower flare half angle of 8°. Similarly, the effects of the nosetip radius are studied by considering a blunt cone with a larger nose radius of 1.0 mm at a fixed flare half angle of 10°. Figure 8 shows the comparison of the N-factor envelopes based on the total disturbance energy for the planar and oblique waves with $m = 0$, 10, 20, and 30 for the selected cone-cylinder-flare configurations. The effect of the lower flare half angle is to slightly reduce the amplification of the disturbances along the cylinder as well as the flare. The nosetip bluntness stabilizes planar and oblique waves along the cone, but has limited effect on the downstream behavior of both groups of waves, except for promoting a continued growth of the $m = 20$ waves across the separated region. For $x > 0.4$ m, the N-factors for the blunt cone are lower than those over the sharp cone by at least 3 for $m = 0$, and by as much as 4 for $m = 10$. The blunt-cone reduction in N-factors is much lower for $m = 20$ and the least for the very oblique waves with $m = 30$, where the N-factor differential with respect to the sharp cone case is less than approximately 1.5.

C. Global Instabilities

GSA of the cone-cylinder-cone configuration is performed for flare half angles equal to 8°, 10°, and 12°. To assess the effects of nose bluntness on the global instability, we consider three different values of the nose radius (namely, 0.1, 1, and 5 mm, respectively) at each flare half angle. As the flare half angle is increased, the length as well as the strength of the separation bubble also increases, along with a correspondingly larger reversed flow velocity. The effects of the nosetip bluntness are qualitatively similar to those of the flare angle, with an increasing nose radius resulting in a longer separation bubble with a stronger recirculation. Figure 9 shows the growth rate of the leading global mode as a function of the azimuthal wavenumber for each selected configuration. The flow is seen to be globally unstable for the 10° half-angle flare for each of the three nosetip radii. For the sharp, 10° flare, the largest growth rate corresponds to a stationary disturbance with $m = 5$. The real part of the azimuthal velocity component of the corresponding global mode eigenfunction is plotted in Fig. 9(b). The mode shape is mostly concentrated within the separation region. A similar mode was found in the GSA of a Mach 5 double wedge configuration studied by GS et al. [12] for a compression angle of 8° following an upstream wedge with a 12° half angle. Similar to their case, the global mode that first becomes unstable as the compression angle is increased corresponds to a wavelength to separation-length ratio of 0.26. As the flare half angle is increased significantly above the initial onset of global instability, the azimuthal wavenumber of the most unstable disturbance increases to $m = 25$ for the 12° flare half angle, and the mode shape concentrates in the reattachment region as shown in Fig. 9(c). A similar behavior was predicted by GS et al. [12] for the double wedge

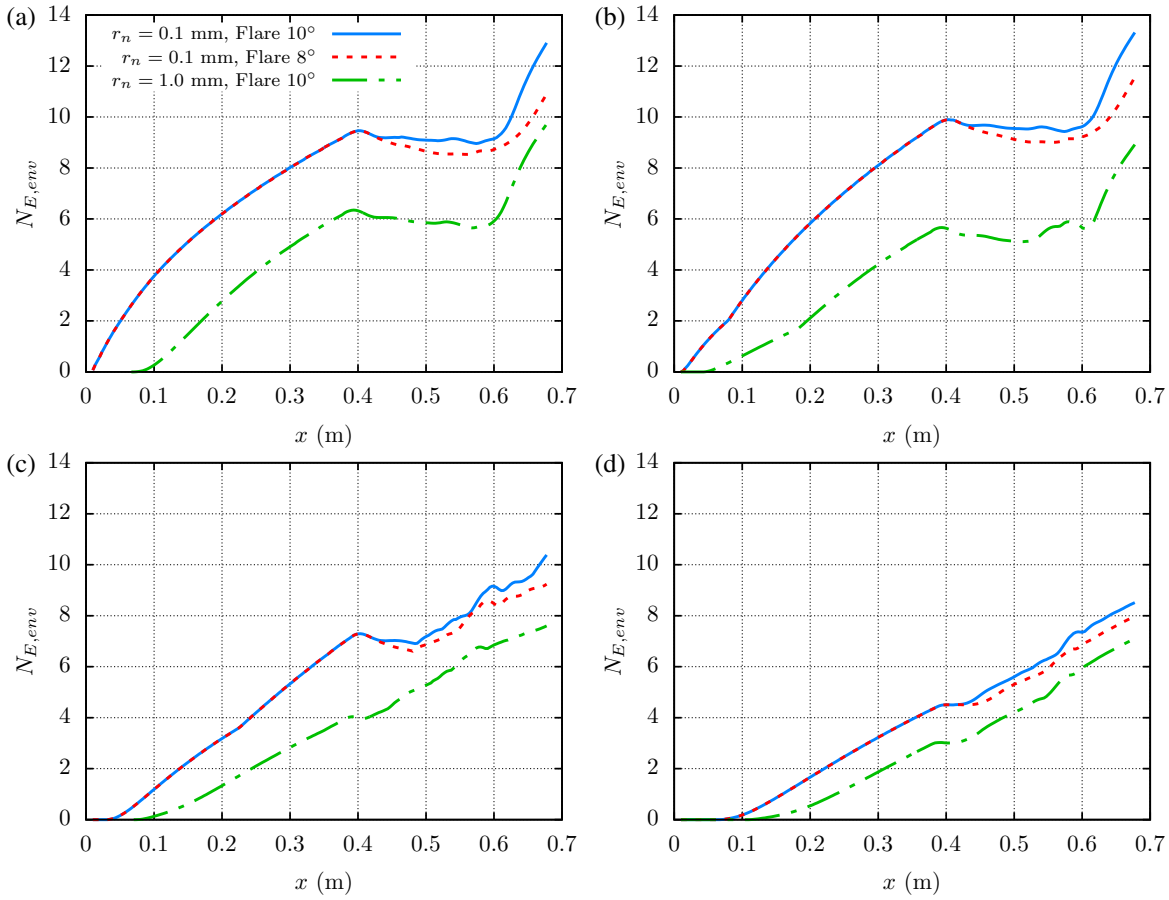

Fig. 8 Evolution of N-factor envelopes based on total disturbance energy ($N_{E,env}$) for the cone-cylinder-flare models with sharp cone ($r_n^* = 0.1$ mm) and flare half angles of $8°$ and $10°$ and a blunt cone ($r_n^* = 1$ mm) with a flare half angle of $10°$. The selected disturbance azimuthal wavenumbers are (a) $m = 0$, (b) $m = 10$, (c) $m = 20$, and (d) $m = 30$.

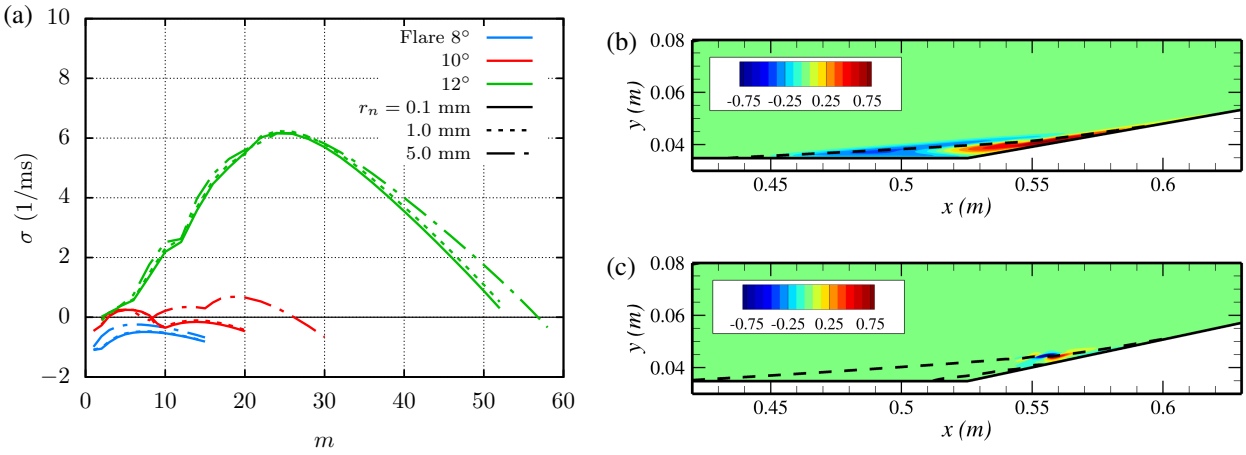

Fig. 9 (a) Growth rate of leading global mode as a function of the flare half angle and nosetip radius. (b,c) Real part of azimuthal velocity component of the disturbance amplitude function $\hat{\mathbf{q}}$, normalized with $\max(|\hat{w}|)$, for the sharp cone ($r_n^* = 0.1$ mm). Part (b) corresponds to the most unstable global mode ($m = 5$) with $10°$ half-angle flare and part (c) to the most unstable global mode ($m = 25$) with $12°$ half-angle flare. The black dashed lines corresponds to the separation lines, $\bar{u} = 0$.

configuration as the compression angle is increased from 8° to 10°, and the associated spanwise wavelength was found to agree with the experimental measurements of Yang et al. [7] that used the same double-wedge configuration and flow conditions. The nosetip radius of 1 mm is found to have a negligible effect on the leading global modes for the considered flare half angles. However, the 5 mm nosetip radius decreases the decay rate of the least stable global mode for the 8° half-angle flare and increases the peak growth rate for the 10° half-angle flare, displacing the most unstable mode to higher azimuthal wavelengths.

IV. Summary and Concluding Remarks

The present study has investigated the convective and global instability characteristics of the laminar, axisymmetric boundary-layer flow over a cone-cylinder-flare model comprised of a 5° half-angle cone with a nosetip radius equal to 0.1, 1, or 5 mm, a cylinder, and a flare with a half angle of 8°, 10°, of 12°. The sharp nose configuration with a 10° flare half angle corresponds to the wind tunnel configuration used by Benitez et al. [15, 16] for their experiments in the BAM6QT at Purdue University. The flow conditions used herein (namely, a Mach 6.0 flow with a unit Reynolds number of 11.5×10^6 m^{-1}, freestream temperature of 51.4 K, and an isothermal wall temperature of 300 K) have also been selected to allow for a direct comparison with the measured heat flux distribution and the frequency spectra measured by surface pressure transducers.

The parabolized stability equations (PSE) are used to study the linear amplification of planar and oblique modal instabilities over the cone portion of the geometry. To account for the effects of increased mean-flow nonparallelism near the cone-cylinder and cylinder-flare corners and the separation bubble near the latter corner, the harmonic linearized Navier-Stokes equations (HLNSE) are used in conjunction with an inflow condition from the solution of the PSE. The power spectra of the surface pressure fluctuations measured with PCB and Kulite sensors are compared with the predicted amplitude spectra scaled to a uniform initial amplitude at a selected axial location upstream of the cone-cylinder juncture. The distinct lobes of disturbance amplification in the measured spectra are well captured in the computational analysis, but some quantitative differences in the amplification characteristics are seen at low frequencies. While the measurements cannot distinguish between planar and oblique disturbances, the computations reveal that the oblique disturbances are more amplified than the planar disturbances. Oblique disturbances in the frequency range of 30 kHz to 150 kHz amplify along the shear layer over the separation region. The computations reveal that both planar and oblique disturbances within the second mode frequency range of 180 kHz to 250 kHz are strongly stabilized in the expansion region near the cone-cylinder corner, but they begin to amplify again at the reattachment location. The amplification of boundary-layer instabilities along the cylinder-flare region is reduced when the flare half angle is reduced. Similarly, increasing nosetip bluntness is found to stabilize the disturbances along the cone section because of the induced entropy layer but is found to have a limited effect along the cylinder-flare region. A global stability analysis (GSA) is also

performed for the selected configurations. The critical flare angle for the onset of global instability is identified as between 8° and 10°. The maximum growth rate of the global modes for the 10° flare configuration corresponds to a stationary three-dimensional instability with an azimuthal wavenumber of 5. As the flare angle is increased to 12°, the most unstable global mode becomes a stationary disturbance with an azimuthal wavenumber of 25 and concentrates in the reattachment region. The nosetip bluntness is found to destabilize the global modes for 8° and 10° half-angle flares, while a rather limited effect is found for the supercritical flare configuration with a 12° half-angle flare. The overall significance of these global modes is beyond the scope of the linear stability analysis considered herein; however, the general agreement between the predicted spectra of the convective instability modes and the measured spectra of the surface pressure fluctuations suggests that the global modes may not exert a major influence on the overall evolution of the convective modes.

Acknowledgments

This material is based upon research supported in part by the U. S. Office of Naval Research under award number N00014-20-1-2261 and in part by the Hypersonic Technology Project (HTP) under the Aeronautics Research Mission Directorate (ARMD). The computational resources supporting this work were provided by the DoD High Performance Computing Modernization Program, the NASA High-End Computing (HEC) Program through the NASA Advanced Supercomputing (NAS) Division at Ames Research Center and the LaRC K-Midrange Cluster at Langley Research Center. The authors would like to thank Drs. Steven Schneider, Sebastien Esquieu, and Joseph Kuehl for technical discussions related to this topic.

References

[1] Becker, J., and Korycinsky, P., "Heat Transfer and Pressure Distribution at a Mach Number of 6.7 on Bodies with Conical Flares and Extensive Flow Separation," Tech. Rep. RM L56F22, NACA, 1956. DTIC citation AD0274584.

[2] Chapman, D., Kuehn, D., and Larson, H., "Investigation of Separated Flows in Supersonic and Subsonic Streams with Emphasis of the Effect of Transition," Tech. Rep. TR 1356, NACA, 1958. NTRS number 19930092343.

[3] Schaefer, J., and Ferguson, H., "Investiation of Separation and Associated Heat Transfer and Pressure Distribution on Cone-Cylinder-Flare Configurations at Mach Five," *ARS Journal*, Vol. 32, No. 5, 1962, pp. 762–770. doi:10.2514/8.6146.

[4] Running, C., Juliano, T., Jewell, J., Borg, M., and Kimmel, R., "Hypersonic Shock-Wave/boundary-Layer Interactions on a Cone/flare," *Experimental Thermal and Fluid Science*, Vol. 109, 2019, p. 109911. doi:10.1016/j.expthermflusci.2019.109911.

[5] Ginoux, J., "Investigation of Flow Separation Over Ramps at $M_\infty = 3$," Tech. Rep. AEDC-TR-65-273, Von Karman Gas Dynamics Facility, Arnold Engineering Developement Center, 1965.

[6] Benay, R., Chanetz, B., Mangin, B., and Vandomme, L., "Shock Wave/transitional Boundary-Layer Interactions in Hypersonic Flow," *AIAA Journal*, Vol. 44, No. 6, 2006, pp. 1243–1254. doi:10.2514/1.10512.

[7] Yang, L., Zare-Behtash, H., Erdem, E., and Kontis, K., "Investigation of the Double Ramp in Hypersonic Flow using Luminescent Measurement Sytems," *Experimental Thermal and Fluid Science*, Vol. 40, 2012, pp. 50–56. doi:10.1016/j.expthermflusci.2012.01.032.

[8] Roghelia, A., Olivier, H., Egorov, I., and Chuvakhov, P., "Experimental Investigation of Görtler Vortices in Hypersonic Ramp Flows," *Experiments in Fluids*, Vol. 58, No. 139, 2017, pp. 1–15. doi:10.1007/s00348-017-2422-y.

[9] Running, C., Juliano, T., Borg, M., and Kimmel, R., "Characterization of Post-Shock Thermal Striations on a Cone/flare," *AIAA Journal*, Vol. 58, No. 5, 2020, pp. 2352–2358. doi:10.2514/1.J059095.

[10] Robinet, J.-C., "Bifurcations in Shock-Wave/laminar-Boundary-Layer Interaction: Global Instability Approach," *J. Fluid Mech.*, Vol. 579, 2007, pp. 85–112. doi:10.1017/S0022112007005095.

[11] Hildebrand, N., Dwivedi, A., Nichols, J., Jovanović, M., and Candler, G., "Simulation and Stability Analysis of Oblique Shock-Wave-Boundary-Layer Interactions at Mach 5.92," *Physical Review Fluids*, Vol. 3, No. 013906, 2018. doi:10.1103/PhysRevFluids.3.013906.

[12] GS, S., Dwivedi, A., Candler, G., and Nichols, J., "Onset of Three-Dimensionality in Supersonic Flow Over a Slender Double Wedge," *Physical Review Fluids*, Vol. 3, No. 093901, 2018. doi:10.1103/PhysRevFluids.3.093901.

[13] Lugrin, M., Beneddine, S., Leclercq, C., Garnier, E., and Bur, R., "Transition Scenario in Hypersonic Axisymmetrical Compression Ramp Flow," *J. Fluid Mech.*, Vol. 907, No. A6, 2021. doi:10.1017/jfm.2020.833.

[14] Esquieu, S., Benitez, E., Schneider, S., and Brazier, J.-P., "Flow and Stability Analysis of a Hypersonic Boundary-Layer Over an Axisymmetric Cone-Cylinder-Flare Configuration," AIAA Paper 2019-2115, 2019.

[15] Benitez, E., Jewell, J., Schneider, S., and Esquieu, S., "Instability Measurements on an Axisymmetric Separation Bubble at Mach 6," AIAA Paper 2020-3072, 2020.

[16] Benitez, E., Jewell, J., and Schneider, S., "Separation Bubble Variation Due to Small Angles of Attack for an Axisymmetric Model at Mach 6," AIAA Paper 2021-0245, 2021.

[17] Butler, C., and Laurence, S., "Interaction of Hypersonic Boundary-Layer Instability Waves with Asixymmetric Compression and Expansion Corners," AIAA Paper 2020-3071, 2020.

[18] Paredes, P., Choudhari, M., Li, F., Jewell, J., Kimmel, R., Marineau, E., and Grossir, G., "Nosetip Bluntness Effects on Transition at Hypersonic Speeds: Experimental and Numerical Analysis," *Journal of Spacecraft Rockets*, Vol. 56, No. 2, 2019.

[19] Chu, B.-T., "On the Energy Transfer to Small Disturbances in Fluid Flow (PART I)," *Acta Mechanica*, Vol. 1, No. 3, 1956, pp. 215–234.

[20] Mack, L. M., "Boundary Layer Stability Theory," Tech. Rep. Jet Propulsion Laboratory Report 900-277, California Institute of Technology, Pasadena, CA, 1969.

[21] Saad, Y., "Variations of Arnoldi's Method for Computing Eigenelements of Large Unsymmetric Matrices," *Linear Algebra Applications*, Vol. 34, 1980, pp. 269–295. doi:10.1016/0024-3795(80)90169-X.

[22] Hermanns, M., and Hernández, J., "Stable High-Order Finite-Difference Methods Based on Non-Uniform Grid Point Distributions," *International Journal for Numerical Methods in Fluids*, Vol. 56, 2008, pp. 233–255. doi:10.1002/fld.1510.

[23] Paredes, P., Hermanns, M., Le Clainche, S., and Theofilis, V., "Order 10^4 Speedup in Global Linear Instability Analysis using Matrix Formation," *Computer Methods in Applied Mechanics and Engineering*, Vol. 253, 2013, pp. 287–304. doi: 10.1016/j.cma.2012.09.014.

[24] Schneider, S., "Development of Hypersonic Quiet Tunnels," *Journal of Spacecraft Rockets*, Vol. 45, No. 4, 2007, pp. 641–664. doi:10.2514/1.34489.

[25] Litton, D., Edwards, J., and White, J., "Algorithmic Enhancements to the VULCAN Navier-Stokes Solver," AIAA Paper 2003-3979, 2003. doi:10.2514/6.2003-3979.